Four-α-Helix Bundle with Designed Anesthetic Binding Pockets. Part I: Structural and Dynamical Analyses

Dejian Ma,* Nicole R. Brandon,* Tanxing Cui,* Vasyl Bondarenko,* Christian Canlas,* Jonas S. Johansson,[§¶] Pei Tang,*[†‡] and Yan Xu*[†]

*Department of Anesthesiology, [†]Department of Pharmacology, and [‡]Department of Computational Biology, University of Pittsburgh School of Medicine, Pittsburgh, Pennsylvania, 15260; [§]Department of Anesthesiology and Critical Care, and [¶]Johnson Research Foundation, Department of Biochemistry and Biophysics, University of Pennsylvania, Philadelphia, Pennsylvania 19104

ABSTRACT The four-α-helix bundle mimics the transmembrane domain of the Cys-loop receptor family believed to be the protein target for general anesthetics. Using high resolution NMR, we solved the structure (Protein Data Bank ID: 2I7U) of a prototypical dimeric four-α-helix bundle, $(A\alpha_2\text{-L1M/L38M})_2$, with designed specific binding pockets for volatile anesthetics. Two monomers of the helix-turn-helix motif form an antiparallel dimer as originally designed, but the high-resolution structure exhibits an asymmetric quaternary arrangement of the four helices. The two helices from the N-terminus to the linker (helices 1 and 1′) are associated with each other in the dimer by the side-chain ring stacking of F12 and W15 along the long hydrophobic core and by a nearly perfect stretch of hydrophobic interactions between the complementary pairs of L4, L11, L18, and L25, all of which are located at the heptad *e* position along the helix-helix dimer interface. In comparison, the axes of the two helices from the linker to the C-terminus (helices 2 and 2′) are wider apart from each other, creating a lateral access pathway around K47 from the aqueous phase to the center of the designed hydrophobic core. The site of the L38M mutation, which was previously shown to increase the halothane binding affinity by ~3.5-fold, is not part of the hydrophobic core presumably involved in the anesthetic binding but shows an elevated transverse relaxation (R_2) rate. Qualitative analysis of the protein dynamics by reduced spectral density mapping revealed exchange contributions to the relaxation at many residues in the helices. This observation was confirmed by the quantitative analysis using the Modelfree approach and by the NMR relaxation dispersion measurements. The NMR structures and Autodock analysis suggest that the pocket with the most favorable amphipathic property for anesthetic binding is located between the W15 side chains at the center of the dimeric hydrophobic core, with the possibility of two additional minor binding sites between the F12 and F52 ring stacks of each monomer. The high-resolution structure of the designed anesthetic-binding protein offers unprecedented atomistic details about possible sites for anesthetic-protein interactions that are essential to the understanding of molecular mechanisms of general anesthesia.

INTRODUCTION

Recent mutagenesis and biophysics investigations have led to the belief that general anesthetics, although structurally diverse, can interact with proteins in a specific manner (1–7). Among the proteins that are essential for neurological functions, a superfamily of neurotransmitter-gated postsynaptic receptors, known as the Cys-loop receptors, has been shown to be particularly sensitive to volatile anesthetics (8). The Cys-loop receptors are ion channels that, on activation by neurotransmitter binding, respond to fast synaptic transmissions in the central and peripheral nervous systems (9). These ion channels are formed by association of five subunits, each of which has four transmembrane (TM) domains, traversing the membrane four times as a four-α-helix bundle. Point mutations in the TM domains of the Cys-loop receptors have been found to significantly alter the receptors' sensitivity to volatile anesthetics (10), implicating certain specific interactions between the anesthetics and the TM four-α-helix bundles.

Despite numerous functional investigations, the current knowledge on the structure-function relationship of anesthetic-protein interactions is limited. This is largely because of the technical difficulties in studying membrane proteins. Although significant progress has been made in recent years (11–17), no structure at the atomistic resolution is currently available for the four-α-helix bundle TM domains of the Cys-loop receptors.

To understand the structural basis of anesthetic-protein interactions, de novo designs of prototype four-α-helix bundles with specific anesthetic binding pockets have been proposed (18,19). The original design, denoted as $(L\alpha_2)_2$, was composed of a Leu-rich hydrophobic core as part of an anesthetic binding pocket. The pocket was later modified with six Leu-to-Ala mutations (denoted as $(A\alpha_2)_2$), leading to a factor of 4.4 improvement in the halothane binding affinity. Further optimization with an additional 3.5-fold binding affinity increase was achieved in $(A\alpha_2)_2$ with the L38M point mutation (19). This newer generation four-α-helix bundle protein has a halothane dissociation constant, K_d, of 0.2 mM, which is essentially the same as the clinical concentration for halothane. Thus, $(A\alpha_2\text{-L38M})_2$ is considered one of the most

Submitted July 19, 2007, and accepted for publication January 18, 2008.

Address reprints to Professor Yan Xu or Professor Pei Tang, 2048 Biomedical Science Tower 3, 3501 Fifth Avenue, Pittsburgh, PA 15260. Tel.: 412-648-9922; Fax: 412-648-8998; E-mail: xuy@anes.upmc.edu or tangp@anes.upmc.edu.

Editor: Susan P. Gilbert.

0006-3495/08/06/4454/10 $2.00

doi: 10.1529/biophysj.107.117838

suitable models for the volatile anesthetic binding targets in the four-α-helix bundle scaffold proteins.

Because of the size difference between the Leu and Ala side chains, the improvement in anesthetic binding due to the Leu-to-Ala mutations in $(A\alpha_2)_2$ was interpreted intuitively as the result of the steric effects, namely, a possibly better fit between anesthetic molecules and their binding pockets. Nearly the same degree of improvement seen in the L38M mutation, however, was not expected fully by design. Molecular dynamics simulations of a structure model for $(A\alpha_2$-L38M$)_2$ showed that M38 was not even part of the hydrophobic core (20), suggesting that factors other than simple geometric fitting or steric restrictions between anesthetic molecules and protein pockets might be at play in determining the anesthetic binding affinity. To better understand these factors, we determined the high-resolution structure and dynamics of the bacterial-expressed $(A\alpha_2$-L1M/L38M$)_2$, which has compatible anesthetic-binding properties to the early chemically synthesized $(A\alpha_2$-L38M$)_2$ (21). The sequence of this 62-residue peptide and the heptad repeat assignments used to design the amphiphilic α-helices are shown in Fig. 1. We present here the results of our investigation in the absence of any anesthetic binding and emphasize the intrinsic structural and dynamical properties of this designed anesthetic-binding protein. The parallel studies of the same protein in the presence of halothane are presented in our Part II article in this issue (22).

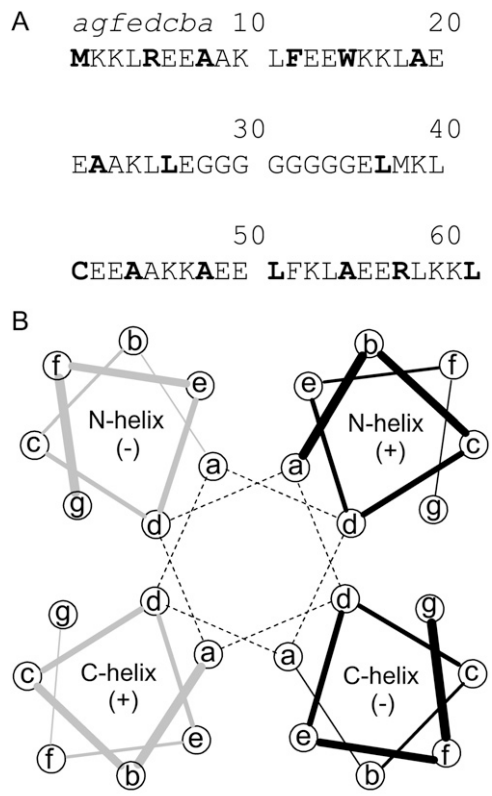

FIGURE 1 (*A*) The primary structure of $(A\alpha_2$-L1M/L38M$)_2$ four-α-helix bundle protein with the heptad position *a* and *d* positions highlighted in boldface. (*B*) Wheel diagram showing a single cycle of the heptad repeat. The left two helices belong to a monomer (*gray*) with the linker below the plane of the page, and the right two helices belong to another monomer (*black*) with the linker above the plane of the page. The direction of the helices is indicated by the + and – signs. The *a* and *d* positions on the helices form the hydrophobic core of the four-α-helix bundle.

MATERIALS AND METHODS

Sample preparation

$(A\alpha_2$-L1M/L38M$)_2$ was expressed using BL21 codon plus (DE3)-RP competent *Escherichia coli* cells in M9 minimal media and purified using reversed-phase HPLC, as described previously (21). The L1M mutation was required for the bacteria to express the protein without a fusion protein. The M9 medium contained $(^{15}NH_4)_2SO_4$ and ^{13}C-glucose as the sole ^{15}N and ^{13}C sources for uniform ^{15}N and ^{13}C labeling, respectively. The purified protein was lyophilized and stored at –20°C until use. NMR samples were prepared by dissolving lyophilized protein in a 10% D_2O/90% H_2O solution to a monomer concentration of 0.5 mM in a total volume of 300–400 μL. Approximately 1 μL of 100 mM 2,2-dimethyl-2-silapentane-5-sulfonate (DSS) sodium salt was added as an internal chemical shift reference. Typically, the unbuffered sample has a pH of 4.5. Samples prepared in this way have been stable for several months if stored at 4°C.

NMR experiments

A suite of two-dimensional and three-dimensional (3D) NMR experiments for spectral assignment, including ^{1}H-^{15}N HSQC, HNCO, HNCA, HN(CO)CA, HNCACB, CBCA(CO)NH, HBHANH, and HBHA(CO)NH, was performed at 35°C using a Bruker Avance 600 MHz spectrometer equipped with a cryoprobe (Bruker Instruments, Billerica, MA). The ^{13}C-decoupled ^{1}H-^{15}N HSQC was acquired in 1024 (^{1}H) $\times$ 128 (^{15}N) complex points, with a spectral width of 10 ppm for ^{1}H and 23 ppm for ^{15}N, and averaged for 16 scans. The HNCACB was acquired in 512 (^{1}H) $\times$ 24 (^{15}N) $\times$ 64 (^{13}C) complex points, with spectral widths of 10 ppm (^{1}H), 22 ppm (^{15}N), and 64 ppm (^{13}C), and 32 scans. The CBCA(CO)NH, HNCO, HNCA, and HN(CO)CA were each acquired in 512 (^{1}H) $\times$ 30 (^{15}N) $\times$ 64 (^{13}C) complex points, with spectral widths of 10 ppm (^{1}H) and 22 ppm (^{15}N), and 16 scans. The ^{13}C spectral widths were 64 ppm (CBCA(CO)NH), 20 ppm (HNCO and HNCA), or 24 ppm (HN(CO)CA).

The 3D HCCH-TOCSY was acquired at 35°C on a Bruker Avance 700 MHz spectrometer with a cryoprobe using the following parameters: 1024(^{1}H) $\times$ 64(^{13}C) $\times$128(^{1}H-indirect) points, spectral widths of 10 ppm for ^{1}H and 75 ppm for ^{13}C, carrier at H_2O resonance for ^{1}H and 41.65 ppm for ^{13}C, and 16 transients for each time increment. To assist with manual assignments and to obtain distance constraints for the structure calculation, ^{15}N-edited 3D NOESY (mixing time of 120 ms and 150 ms) and ^{13}C-edited 3D NOESY (mixing time of 75 ms and 150 ms) were performed. All four NOESY experiments had 512 (^{1}H) $\times$ 30 (^{15}N) $\times$ 64 (^{13}C) complex points and 16 scans. The spectral widths were 10 ppm for ^{1}H, 22 PM for ^{15}N, and 40 ppm for ^{13}C.

To measure the temperature effects, a series of ^{1}H-^{15}N HSQC experiments were performed at 25, 30, 35, and 40°C. The same sample as the one for the assignment experiments was used. The experiments were performed on a Bruker Avance 600 MHz spectrometer with a TXI probe. At least 30 min were given between each temperature change for the sample to equilibrate before proceeding with the experiment. HSQC at 35°C was repeated to verify that the protein had not irreversibly changed at different temperature steps. Each ^{1}H-^{15}N HSQC was acquired with 16 scans in 512 (^{1}H) $\times$ 64 (^{15}N) complex points and spectral widths of 10 ppm (^{1}H) and 22 ppm (^{15}N).

The four-α-helix bundle dynamics was measured at 35°C using ^{15}N R_1 and R_2 relaxation and ^{15}N-{^{1}H} heteronuclear NOE experiments. A Bruker

Avance 600 MHz spectrometer with a TXI probe and the Bruker standard pulse sequences were used. In the R_2 measurements, the interpulse delay between two adjacent ^{15}N 180 pulses in the CPMG sequence was 1000 μs (including a 100-μs pulse width), and thus the field strength of the CPMG refocusing pulses was 1.0 kHz. 512 (^1H) × 128 (^{15}N) complex points were taken, interleaving with and without ^1H saturation. The spectral widths were 10 ppm for ^1H and 22 ppm for ^{15}N, with 88 scans for hetNOE and 24 scans for R_1 and R_2 measurements. The R_1 was determined using 8 delay values: 20, 50, 100, 200, 400, 600, 1100, 2000 ms. The R_2 experiments used eight delay values: 17, 34, 51, 68, 85, 119, 153, 221 ms. The relaxation rate constants were obtained by exponential fitting. The hetNOE values were defined as the ratios of peak intensities with and without proton saturation. The uncertainties of hetNOE values, ΔNOE, were calculated using the well-established method (23):

$$\frac{\Delta NOE}{NOE} = \sqrt{\left(\frac{\Delta I_{\text{sat}}}{I_{\text{sat}}}\right)^2 + \left(\frac{\Delta I_{\text{unsat}}}{I_{\text{unsat}}}\right)^2}, \quad (1)$$

where I_{sat} and I_{unsat} are the peak intensities with and without proton saturation, respectively. Their uncertainties were determined from the root mean-square noise in the background regions.

Data processing and structure calculations

Data were processed using NMRPipe (24) and analyzed with NMRView (One Moon Scientific, Westfield, NJ) (25) or Sparky (26). Because of the repetitive nature of the designed amino acid sequence, the backbone spectral assignments were done semimanually with the aid of the automatic spectral assignment software packages AutoAssign (27) and MONTE (28,29). Structure calculations were performed using CYANA v2.1 (30) based on NOE restraints and Talos dihedral angle restraints from CSI (31). Hydrogen bonding restraints were added for those residues that showed not only slow exchange with water based on the small amide proton chemical shift dependence on temperature (32), but also the helical ^{13}C CSI as well as the helical backbone NOE connectivities. To calculate the dimeric structures, the restraints were duplicated for the two monomers, including 15 intermonomer long-range NOEs observed in the ^{15}N- or ^{13}C-edited NOESY spectra. The intermonomer NOEs were assigned by matching chemical shifts using an exclusion strategy. A total of 100 structures were initially calculated by CYANA. A bundle of 20 structures with the lowest target function is presented. Structures were analyzed using VMD (33) and Molmol (34).

The reduced spectral density mapping method (35) was used to qualitatively evaluate the dynamic characteristics of the protein. The reduced spectral density functions at three frequencies, $J(0)$, $J(\omega_N)$, and $J(0.87\omega_H)$, were calculated from ^{15}N R_1, R_2, and ^{15}N-{^1H} hetNOE by the following matrix conversion (35):

$$\begin{pmatrix} J(0) \\ J(\omega_N) \\ J(0.87\omega_H) \end{pmatrix} = \begin{pmatrix} -0.75\times F & 1.5\times F & -0.9\times F \\ F & 0 & -1.4\times F \\ 0 & 0 & 0.2\times B \end{pmatrix} \times \begin{pmatrix} R_1 \\ R_2 \\ \dfrac{\gamma_N\times(NOE-1)\times R_1}{\gamma_H} \end{pmatrix}, \quad (2)$$

where

$$\frac{1}{B} = \frac{\gamma_{H^N}^2\times\gamma_N^2\times h^2}{4\times r_{NH^N}^6\times 4\pi^2}\times\left(\frac{\mu_0}{4\pi}\right), \quad (3)$$

and

$$\frac{1}{F} = \frac{3}{B} + \frac{\Delta^2\times\omega_N^2}{3}. \quad (4)$$

The ^{15}N-^1H internuclear bond distance (r_{NH}) of 1.02 Å and the ^{15}N chemical shift anisotropy (Δ) of –160 ppm were assumed in the calculation of the matrix elements (35). General classification of the spectral densities was done by comparing the experimental spectral density values with the theoretical curves for the single Lorentzian motion (36):

$$J(0)\times J(\omega) = \frac{J(0)^2}{1+\left[\frac{5}{2}\times\omega\times J(0)\right]^2}. \quad (5)$$

Deviations from the single Lorentzian motion were used to determine qualitatively whether there is an exchange contribution to the relaxation at each residue. In addition, we also employed a similar qualitative method proposed earlier (37) to use $R_1\times R_2$ to effectively discriminate chemical exchange contribution from the motional anisotropy contribution in the R_2 relaxation. This method takes the advantage of the fact that the anisotropy effects on correlation times are greatly attenuated in $R_1\times R_2$ when $\omega\tau \gg 1$. After calculating the theoretical curve of $R_1\times R_2$ as a function of R_2/R_1 using the full spectral density expressions for R_1 and R_2, we compared the experimental data with the theoretical curve in the $R_1\times R_2$ dimension. Any residues with excess $R_1\times R_2$ values above the theoretical curve would suggest a nonzero R_{ex} term for those residues. To quantitatively analyze the ^{15}N relaxation parameters and ^{15}N-{^1H} heteronuclear NOE, the model-free approach (38–41) and the Modelfree program (41) were used. The model selection was first done based on the F-statistics in the R_2/R_1 diffusion analysis. Because qualitative $R_1\times R_2$ vs. R_2/R_1 analysis suggests that many residues have nonzero R_{ex} contribution in the R_2 relaxation (see Results), the global tumbling correlation time (τ_m) was determined by extensive search for the τ_m value that gives the minimum reduced χ^2 value and the least number of nonfitted residues in the Modelfree data fitting, instead of estimating from the R_2/R_1 ratio.

RESULTS

Spectral assignments

As shown in Fig. 1, this designed protein has 14 Es, 12 Ks, 11 Ls, 9 As, 8 Gs, 2 Fs, 2 Ms, 2 Rs, and one C and W, with a significant amount of segment repetitiveness (e.g., 3 EEAAK segments, 7 KL pairs, 6 EE pairs, etc.). Such sequence degeneracy made the NMR spectral assignment difficult. Fig. 2 shows a typical ^1H-^{15}N HSQC spectrum of (Aα_2-L1M/L38M)$_2$. A total of 115 peaks can be found in this spectrum, nearly twice as many as expected. It is clear that the peaks can be classified into two sets based roughly on the intensities, corresponding to two different conformations. From a suite of triple-resonance NMR experiments, 61 out of the 62 residues (except M1) for the major conformation could be positively identified and assigned (see Supplementary Material, Table S1). The final assignments were marked in Fig. 2. Approximately 90% of the side-chain resonances in the major conformation were assigned by using the 3D HCCH-TOCSY. Because many peaks in the 3D spectra for the minor conformation are too weak to be measured, only ~50% of

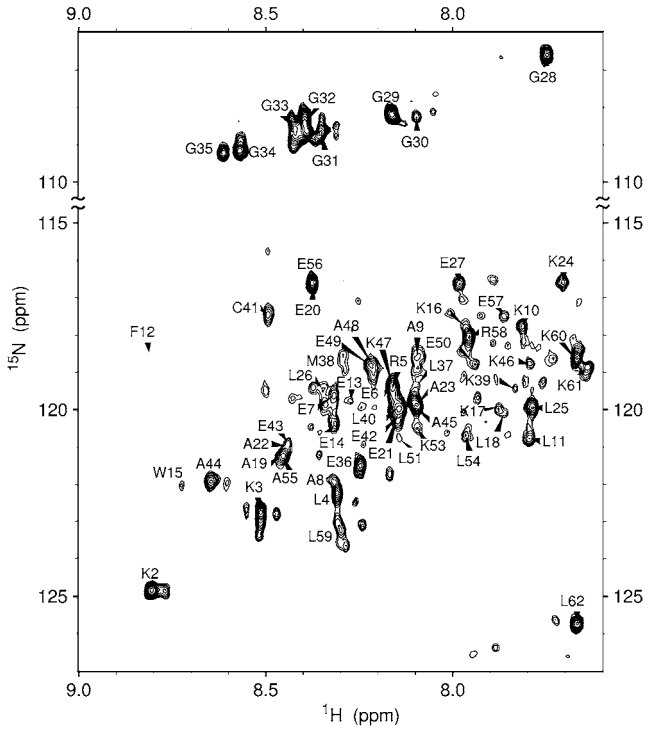

FIGURE 2 [^{1}H, ^{15}N]-HSQC of ^{13}C/^{15}N-labeled four-α-helix bundle in 90% H_2O/10% D_2O with a monomer concentration of 0.5 mM at 35°C and pH 4.5. Sixty-one of 62 backbone resonances of the major conformation are assigned with the exception of M1. F12 is visible when the contour level is lowered. On addition of anesthetics, these resonances become stronger, which allows their assignments to be easily confirmed in 3D experiments. Assignments of the major conformation are labeled using the one-letter amino acid code and the sequence number.

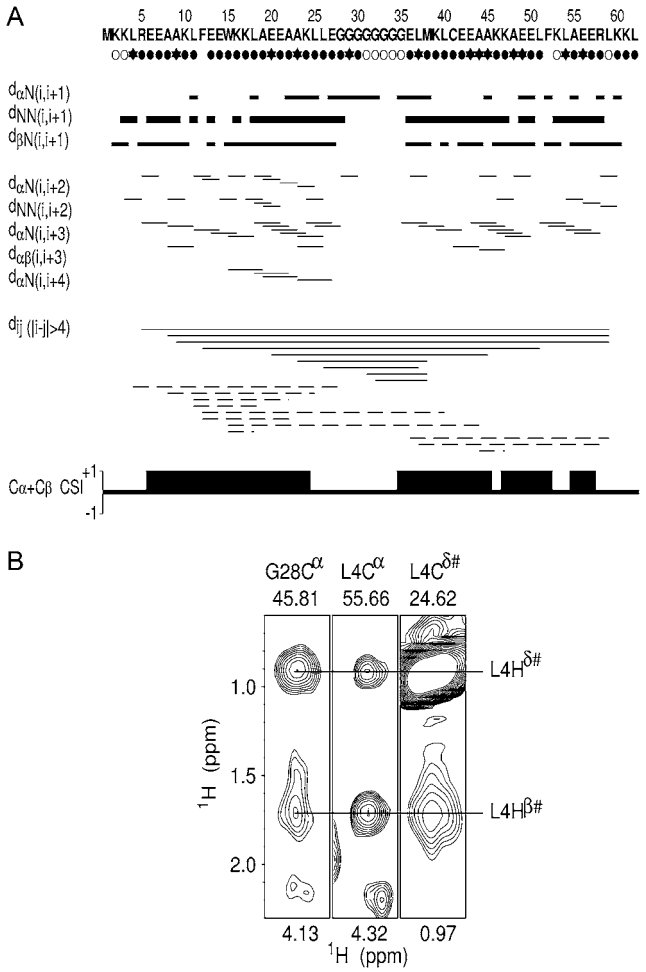

FIGURE 3 (*A*) Summary of NMR restraints determined for ($A\alpha_2$-L1M/L38M)$_2$ four-α-helix bundle. Sequential and midrange NOE connectivity is linked by the line segments, with the line thickness proportional to the crosspeak intensity. For the long-range NOE [$dij(|i-j| > 4)$], the solid lines represent intramonomer NOEs, and the dashed lines represent intermonomer NOEs. The chemical shift index obtained from combining C_α and C_β shifts is also shown. The amide proton chemical shift dependence on temperature is marked under the sequence. Solid circle, solid star, and open circle represent slow, medium, and fast exchange, respectively. (*B*) An example of intersubunit NOESY assignment. Shown here are strip plots from ^{13}C-edited 3D NOESY showing intersubunit NOE crosspeaks between G28 and L4. Such crosspeaks cannot arise from the same subunit.

reliable assignments for the second set of signals can be made. Therefore, the current NMR data set does not allow a complete structure and dynamics characterization of the minor conformation. Possible sources of some of the minor peaks include residual impurity in the protein preparation, a very small population of the four-α-helix in the monomer state, or different forms of dimers (e.g., parallel instead of antiparallel dimers). In this study, we focus only on the major conformation.

High-resolution structures of four-α-helix bundle

The sequential and midrange NOE connectivity in the major conformation, the chemical shift indices (CSI), and the temperature dependence of amide proton chemical shift are summarized in Fig. 3. Similar to using line segments for short- and mid-range NOEs, long-range NOEs ($|i-j| > 4$) are also indicated by lines connecting the two interacting residues. Solid and dashed lines are used to distinguish the intra- and inter-monomer long-range NOEs, respectively. Two helical segments, from E7 to E27 and from E36 to R58, are clearly discernible from the NOE connectivity. The C_α and C_β CSI confirms that at least the segments from E6 to K24 and from E36 to E57 are helical. The first 5 residues from the N-terminus, the last 5 residues to the C terminus, and 11 residues in the center from L25 to G35 have C_α and C_β chemical shifts not significantly different from the random-coil values. The CSI data also suggest a certain degree of disruption in the α-helicity near F52.

Fig. 4 *A* shows a bundle of 20 structures calculated using the restraints derived from the NMR peaks in the major conformation. The atomic coordinates of the structures have been deposited in Protein Data Bank (PDB: 2I7U). The statistics of the structural calculation are given in Table 1. The overall backbone RMSD, including the flexible and less-

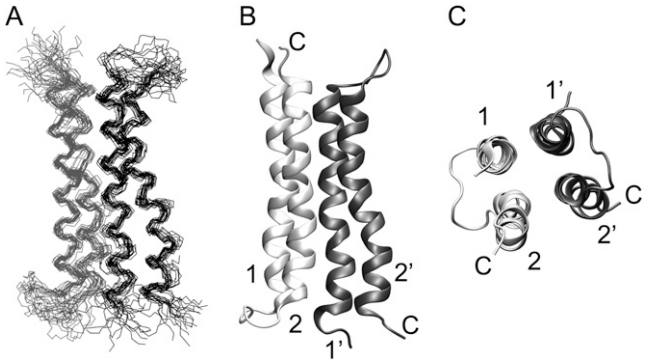

FIGURE 4 (*A*) The backbones of 20 lowest-energy structures of ($A\alpha_2$-L1M/L38M)$_2$, fitted from E6 to E27 and from E36 to E57. Two monomers are colored gray and black for distinction. (*B*) Side view of ($A\alpha_2$-L1M/L38M)$_2$ structure in ribbon representation, showing distortion in helix 2 and helix 2′. (*C*) Top view of ($A\alpha_2$-L1M/L38M)$_2$ structure in ribbon representation. Notice the overall asymmetry in the arrangement of the four helices. The N-terminal helices are labeled as 1 and 1′, and the C-terminal helices as 2 and 2′.

structured terminal and linker regions, is 1.77 ± 0.24 Å. The backbone RMSD for all four helical regions combined is 0.82 ± 0.17 Å. Further improvement of backbone RMSD by residual dipole coupling (RDC) was not attempted because high sequence redundancy and spectral overlap in the IPAP-type spectra would not provide the needed accuracy in the RDC frequency difference measurements.

Several features are readily apparent in the calculated structures: 1), Because of the random-coil structures at the two termini, the helical segments are somewhat shorter than initially designed. 2), The dimer is antiparallel based on the long-range NOEs between the two monomers (Fig. 3, *dashed lines*). 3), There is a super-helical twist (coiled-coil) leading to slight deformation of the helices (Fig. 4 *B*). 4), As originally designed, the first helix from the N-terminus to the linker (helix 1) is associated with the other first helix (helix 1′) in the dimer in an antiparallel fashion (likewise, helix 2 and helix 2′ are associated with each other), such that the hydrophobic surfaces composed of the *a* and *d* positions in the helical heptad are facing each other in the hydrophobic core. 5), The tertiary and quaternary arrangements of the four helices are not completely symmetrical (Fig. 4 *C*). Helices 1 and 1′ are closer to each other than helices 2 and 2′. As will be discussed later, this feature might be essential for creating a lateral pathway for amphiphilic anesthetics to enter the designed hydrophobic core.

TABLE 1 Statistics of 20 NMR structures with the lowest target functions

NMR structure	Statistic
Restraints per monomer	
NOE distances	
Intraresidue	168
Short range (|i–j| = 1)	133
Medium range (1 < | i–j| ≤ 4)	82
Long range (|i–j| > 4)	17
Dimer (intermonomer)	15
Dihedral angles	90
Hydrogen bonds	40
Residual upper limit constraint violations > 0.5 Å	0
Residual dihedral angle constraint violations > 5°	0
Backbone RMSD	
Residues in helical regions only (6–27, 36–58)	0.82 ± 0.17 Å
All residues (1–62)	1.77 ± 0.24 Å
Heavy atom RMSD	
Residues in helical regions only (6–27, 36–58)	1.38 ± 0.20 Å
All residues (1–62)	2.22 ± 0.27 Å
Ramachandran plot	
Residues in most favored regions	92.8%
Residues in allowed regions	6.5%
Residues in disallowed regions	0.7%

Changes in chemical shifts of the amide protons at different temperatures are consistent with both the NOE connectivity and the CSI result. As expected, the slope of chemical shift change with temperature is small for residues in the helical regions, indicating the existence of backbone hydrogen bonding (32), whereas those with large chemical shift changes with temperature are in the glycine linker region. Among the residues associated with the helices, those whose chemical shifts are least sensitive to temperature tend to be in the hydrophobic core of the protein. These data further validate the spectral assignments and confirm that the four-α-helix bundle is a dimer with hydrophobic faces of the monomers associating with each other to exclude the water in the hydrophobic core.

Backbone dynamics

The R_1, R_2, and hetNOE data for the backbone amide ^{15}N of ($A\alpha_2$-L1M/L38M)$_2$, the reduced spectral density mapping results, the R_2/R_1 ratio, and the graphical analyses of $J(\omega_N)$ as a function $J(0)$ and $R_1 \times R_2$ as a function of R_2/R_1 are shown in Fig. 5. The dynamics in the two termini and the loop regions are significantly different from that in the helices. The R_1 values cluster in the 1.8–2.3 s^{-1} range throughout the sequence, with only small variations in the loop region and near the termini. In contrast, R_2 and hetNOE values are significantly smaller in these regions (3.0–6.3 s^{-1}) than in the helices (10.1–13.7 s^{-1}), suggesting considerable backbone flexibility in the loop and the termini. Two residues, M38 and C41, have noticeably higher R_2 values than their adjacent residues (17.5 and 17.3 s^{-1}, respectively), indicating considerable contributions from exchange in the R_2 relaxation for these residues. The hetNOE values are above 0.7 for all residues in the α-helical regions. Initial estimates of the τ_m value of the four-α-helix bundle, based on the R_2/R_1 ratio and averaged over the residues in the α-helical regions, is 5.6 ± 0.5 ns at 600 MHz. Because many residues have nonzero R_{ex} contributions to the R_2 relaxation (see below). The τ_m value should be determined independent of the R_2/R_1 ratio.

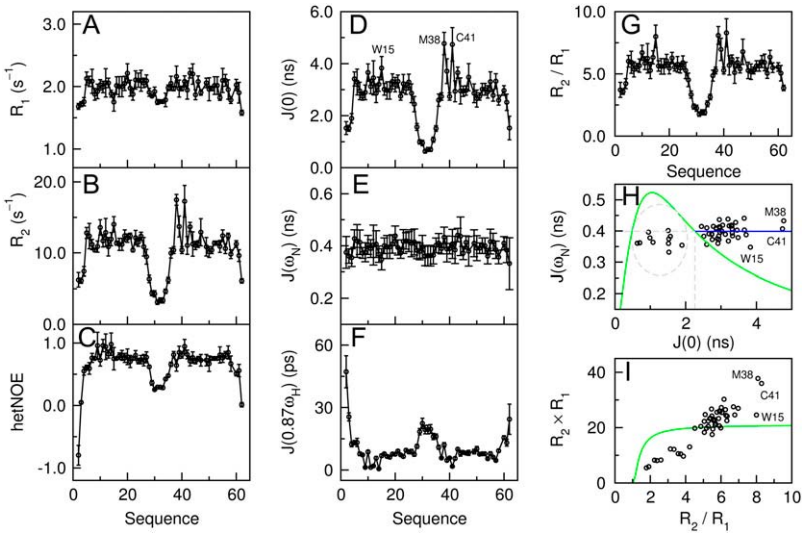

FIGURE 5 Dynamics analysis of the backbone amide ^{15}N of (Aα_2-L1M/L38M)$_2$ in H_2O at 35°C. Longitudinal and transverse relaxation rate constants, R_1 and R_2, and ^{15}N-{^1H} NOE values are shown in *A*, *B*, and *C*, respectively. The reduced spectral density functions, $J(0)$, $J(\omega_N)$, and $J(0.87\omega_H)$, are shown in *D*, *E*, and *F*, respectively. R_2/R_1 ratio and the correlation between $J(\omega_N)$ and $J(0)$ and between $R_1 \times R_2$ and R_2/R_1 are shown in *G*, *H*, and *I*, respectively. The relaxation data were acquired at 600 MHz. Error bars are either the standard errors in the least-squares fit to the exponential decay function (for R_1 and R_2) or the calculated uncertainties (for NOE). (*H*) residues inside the dashed ellipse are from the loop region and the termini. The solid green curves describe the dependence of $J(\omega_N)$ on $J(0)$ in the limiting case of single Lorentzian motion. Points to the right of the green curve suggest the presence of exchange and/or anisotropic contribution to the relaxation. (*I*) the contribution of exchange and anisotropy can be effectively isolated because the dependence of $R_1 \times R_2$ on correlation times is greatly attenuated. Experimental data above the theoretical curve (*solid green curve*) suggest the presence of R_{ex} contribution to the R_2 relaxation.

Qualitative analysis of the relaxation data using the reduced spectral density mapping method clearly indicates a complex dynamics profile of the dimeric (Aα_2-L1M/L38M)$_2$. The points within the dashed ellipse in Fig. 5 *H* are those from the loop and terminal residues, which are less structured and highly flexible. Many residues in the helices exhibit a rightward shift from the theoretical single Lorentzian $J(\omega_N)$ vs. $J(0)$ curve, which is equivalent to the case of isotropic tumbling in the model-free analysis. The rightward shift is an indication that other motions, either anisotropic motion and/or chemical and conformational exchange, contribute to the R_2 relaxation in addition to the global tumbling and internal local motion. Since $J(\omega_N)$ is dominated by R_1 and hetNOE and is independent of R_{ex} (see Eq. 2), the intersection between the single Lorentzian curve and the average $J(\omega_N)$ values (horizontal line in Fig. 5 *H*) yields a $J(0)$ value corresponding to an apparent correlation time should the protein tumble isotropically. This estimate also gives a τ_m value of ~5.6 ns. To distinguish exchange from anisotropy contributions, we compared experimental $R_1 \times R_2$ with the corresponding theoretical values (Fig. 5 *I*). If $R_{ex} = 0$, the experimental $R_1 \times R_2$ would be smaller than the theoretical values by a factor of S^4, where S^2 is the generalized order parameter. A nonzero R_{ex} would displace the experimental values vertically by $R_1 \times R_{ex}$. As shown in Fig. 5 *I*, many residues have nonzero R_{ex} contributions to R_2, with M38 and C41 being distinctly different from the others. We confirmed the presence of exchange contribution to relaxation by the R_2 dispersion measurements, in which the relaxation-compensated, constant-time Carr-Purcell-Meiboom-Gill (CPMG) sequences (42,43) were used to determine the R_2 dependence on the CPMG frequency. Detailed analyses of the relaxation dispersion data and of the anesthetic effects on the conformational exchange are discussed in Part II (22). Quantitative analyses using the Lipari-Szabo model-free approach with the NMR structure and the relaxation data as input are depicted in Fig. 6. The model selection criteria based on F-statistics suggested that the isotropic tumbling model fit the relaxation data of the apo protein better than the anisotropic model. In agreement with the qualitative assessment, the majority of residues in the helical region can be fit best with

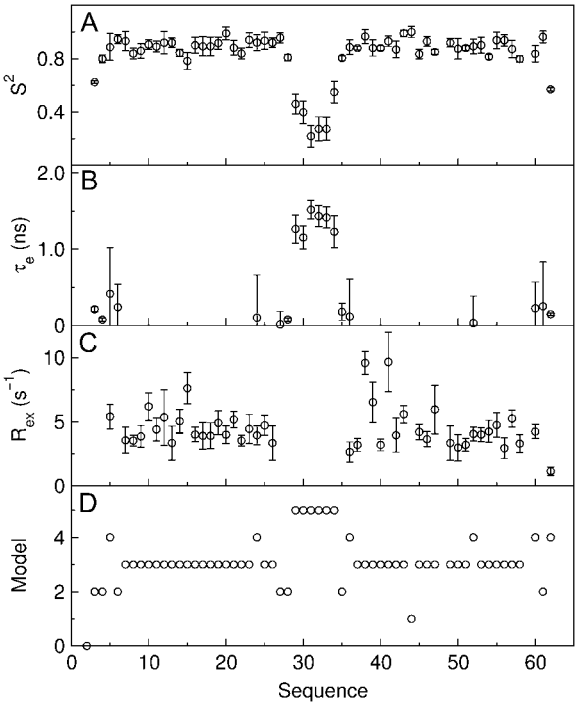

FIGURE 6 Quantitative model-free analyses of the dynamics of (Aα_2-L1M/L38M)$_2$ using Modelfree program: (*A*) the generalized squared-order parameter (S^2); (*B*) the local correlation time (τ_e), (*C*) the exchange term (R_{ex}), and (*D*) the models used to fit the data for each residue. Error bars are standard errors from the fitting.

Model 3, which includes a nonzero R_{ex} term indicative of exchange contribution to the dynamics. Again, the most noticeable dynamical hotspot is the large R_{ex} term for residues M38 and C41, suggesting that the L38M mutation that renders a 3.5-fold increase in halothane binding affinity is at an intrinsically dynamic site of the protein. Note also that the entire loop region can be described only by Model 5, which assumes internal backbone motions on multiple timescales. Thus, the basic assumption for the model-free approach does not strictly apply to the residues in the loop region. By searching for the τ_m value that gives the minimum reduced χ^2 value and the least number of nonfitted residues, Modelfree calculations yielded a global tumbling time of 5.1 $\pm$ 0.1 ns, corresponding to a protein size of 11–12 kDa. Because the (Aα_2-L1M,L38M) monomer has a molecular mass of 6.86 kDa, the dynamics data confirm that the major peaks used for the model-free calculations indeed arise from the dimeric form of the four-α-helix bundle.

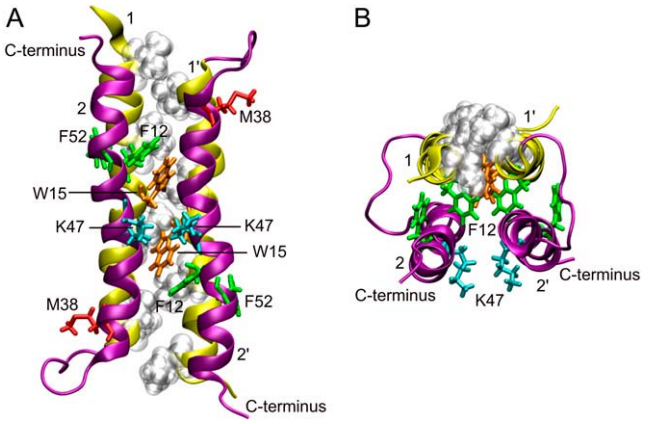

FIGURE 7 Side view (*A*) and top view (*B*) of the (Aα_2-L1M/L38M)$_2$ structure in ribbon representation, showing the relationship of important side chains. Helices 1 and 1′ are colored in yellow and helices 2 and 2′ are colored in purple. The complementary L4, L11, L18, and L25 are depicted in gray in van der Waals spheres representation. F12, F52, W15, M38, and K47 are shown in licorice representation. F12 and F52 are shown in green, W15 in orange, M38 in red, and K47 in cyan.

DISCUSSION

We have solved the high-resolution structure of a designed dimeric four-α-helix-bundle protein that was found previously to interact specifically with volatile anesthetics with relatively high binding affinities. Since the four-α-helix bundle is a ubiquitous scaffold in functional proteins, our designed protein is considered to be a suitable model for anesthetic binding targets. The high and specific anesthetic binding affinity to (Aα_2-L1M/L38M)$_2$ suggests that certain intrinsic structural and dynamical features of this particular protein are essential for volatile anesthetic-protein interaction. Our NMR structure and the dynamics data have revealed some of these features that might be important for anesthetic-protein interaction in general.

Spatial asymmetry of the four helices

An unexpected feature in the high-resolution structure is the overall asymmetry in the spatial arrangement of the four helices. Although the final structures show a two-fold symmetry, which is consistent with the fact that the NMR peaks in the helical region give a tumbling rate of a dimer and that each peak arises from the same residue in the two monomers, the quaternary arrangement of helices 1 and 1′ is different from that of helices 2 and 2′, as shown in Fig. 4 *C*. Careful examinations of the detailed side-chain packing of helices 1 and 1′ shows a stack of aromatic rings from two F12 and two W15 residues in the hydrophobic core, as shown in Fig. 7 *A*. Moreover, there is excellent steric complementarity of eight leucine residues (L4, L11, L18, and L25), all of which occupy the heptad *e* position at the interface of helices 1 and 1′ (Fig. 7 *A*). The accumulation of van der Waals interactions, in addition to the hydrophobic interactions, holds helices 1 and 1′ together in an antiparallel fashion. In contrast, helices 2 and 2′ are wider apart from each other. The complementarity between the hydrophobic side chains of helices 2 and 2′ is disrupted in the middle of the helical interface because K47 is at the heptad *e* position. The side chains of the two K47 collide at nearly the same level (see Fig. 7). The electrostatic repulsion of the charged side chains forces helix 2 to distort slightly. Deformation of helix 2 is also clearly evident in the CSI result in Fig. 3.

Lateral accessibility to binding site

It is very likely that the two K47 in the middle of helix 2 play an important role in the high-affinity anesthetic binding in this designed four-α-helix bundle. One of the most essential properties of general anesthetics is their tendency to preferentially interact with amphipathic molecular targets (4,44,45). As shown in Fig. 7, two K47 residues in the dimeric (Aα_2-L1M/L38M)$_2$ are at the level midpoint to the two W15 side chains. This creates an ideal amphipathic environment. Most importantly, the opening in the middle of the helices 2 and 2′ interface creates a lateral access pathway for anesthetics from the aqueous phase to enter the site between the two W15 side chains in the center of the long hydrophobic core without passing through either end of the four helix bundle. Thus, the predominant anesthetic binding site, which has now been confirmed experimentally (see Part II (22)), is between the two W15 aromatic side chains, bordered additionally by A44 and A48 at the heptad *a* and *e* positions at the same level. A closer examination of this particular binding pocket also predicts that among the six L-to-A mutations to convert (Lα_2)$_2$ to (Aα_2)$_2$ (18), the two L44A and the two L48A are the most crucial ones responsible for the increase in the halothane binding affinity. The bulkier side chains of leucine would require significantly larger distortion

of helix 2 to accommodate a halothane molecule in this pocket.

Importance of aromatic side chains

It is interesting to further analyze the orientations of aromatic side chains from F12, W15, and F52 in the structure. All three residues are located in the helical region. The intensities of these residues in the HSQC spectrum are significantly weaker than other resonances in the major conformation, indicative of intermediate conformational exchange. It is likely that, in response to helix-2 global movement at the level of K47, W15 side chains adapt different orientations in the hydrophobic core when the cavity between the two W15 side chains is not occupied, as suggested previously by a fluorescence quenching study (21). This re-orientation of the bulky W15 side chains will inevitably affect W15 backbone dynamics. As we have found in the study with halothane (see Part II (22)), the presence of a bound halothane stabilizes the W15 side chains, resulting in not only halothane concentration-dependent shift of W15 backbone amide ^{1}H and ^{15}N resonance, but also an increase in peak intensity for W15 in the HSQC spectrum with halothane. The increases in peak intensity after halothane binding strongly suggest that the weak intensity of W15 in the absence of halothane is indeed the result of intermediate conformation exchange.

In the NMR structure, F52 seems to be ''out of place''. Although it is designed to be at the heptad *g* position, which is supposed to be at the interface between helix 1 and helix 2 of the same monomer, the F52 side chain is extended outward, pointing into the aqueous phase. This is the direct consequence of the helix 2 distortion from K47 to the C-terminus. Having a highly hydrophobic side chain oriented into the aqueous phase is energetically unfavorable. Hence, it is expected that the F52 side chain experiences a tremendous amount of fluctuations, which leads to greatly reduced F52 resonance in HSQC.

Because of its ''odd'' location, the F52 side chain can only be stabilized by the ring stacking with the side chain of F12 in the same monomer. This affords the possibility of another two plausible anesthetic binding sites in $(A\alpha_2\text{-L1M/L38M})_2$, namely, the space sandwiched by the F12 and F52 side chains. However, because of the extremely hydrophobic rather than amphipathic nature of the phenylalanine residues, these two additional anesthetic binding sites would be not as favorable as the major binding site between the two W15 side chains.

Implications of dynamics in anesthetic binding

$(A\alpha_2\text{-L1M/L38M})_2$ exhibits a very interesting motional profile as measured by the ^{15}N backbone dynamics. As shown in Fig. 6, our designed four-α-helix bundle is a very dynamic protein in the absence of a bound anesthetic. Judged by the nonzero R_{ex} terms, it can be concluded that neither of the two helices behave like a rigid rod. Instead, as discernible in the NMR structure, the well known coiled-coil structural twist commonly found in four-α-helix bundles might result from the underlying superhelical twist motion. Indeed, when we subject the NMR structure of $(A\alpha_2\text{-L1M/L38M})_2$ to normal mode analysis using ElNemo (46,47), we found that the global mode (the first nonzero mode) is dominated by a large-amplitude winding and unwinding helical twist motion. Such coiled-coil twist may prove to be the universal dynamic characteristic of four-α-helix bundles. The fact that so many structurally diverse anesthetics can interact with so many proteins in a similar way suggests the possibility of an ''induced fit'' between small volatile anesthetic molecules and their protein targets. The protein's intrinsic ability to be flexible enough to accommodate necessary conformational changes upon anesthetic binding is exemplified in $(A\alpha_2\text{-L1M/L38M})_2$. It is tempting to speculate that the coupling between the supercoil twisting global dynamics and the structurally defined amphipathic lateral pathway leading to the binding pocket will facilitate the binding on-rate when the binding site(s) are empty. As will be shown in the study with anesthetics (see Part II (22)), the presence of halothane in the binding site reduces the dynamics of $(A\alpha_2\text{-L1M/L38M})_2$, thus decreasing the off-rate of the bound halothane. Our structural and dynamic data on the apo protein seem to suggest the possibility of interplay between structural and global dynamics as contributing factors for anesthetic-protein interactions. This possibility is further explored in Part II (22).

In conclusion, to our knowledge, we have solved the first high-resolution structure of a designed anesthetic-binding protein having the common four-α-helix bundle scaffold. In the apo form, the protein is highly dynamic, with a clear indication of conformational heterogeneity on the NMR timescale. The major conformation is an antiparallel dimer showing two helices from the N-terminus to the linker packed neatly with a long stretch of eight complementary leucine side chains at the heptad *e* positions and four aromatic rings in the hydrophobic core. The two helices from the linker to the C-terminus are less well packed because of two charged K47 side chains being too close to each other. The distortion of the second helix from a straight helix creates a lateral access pathway for general anesthetics to reach the amphipathic binding site between the two W15 side chains. The global protein dynamics, coupled with the mobility near the flexible glycine linker, seems to contribute to the specific anesthetic binding affinity to this designed protein.

SUPPLEMENTARY MATERIAL

To view all of the supplemental files associated with this article, visit www.biophysj.org.

This work was supported in part by grants from the National Institutes of Health (R37GM049202 to Y.X. and P.T., R01GM056257 to P.T., and P01GM055876 to Y.X. and J.S.J.).

REFERENCES

1. Tang, P., and Y. Xu. 2002. Large-scale molecular dynamics simulations of general anesthetic effects on the ion channel in the fully hydrated membrane: the implication of molecular mechanisms of general anesthesia. *Proc. Natl. Acad. Sci. USA.* 99:16035–16040.
2. Szarecka, A., Y. Xu, and P. Tang. 2007. Dynamics of firefly luciferase inhibition by general anesthetics: Gaussian and anisotropic network analyses. *Biophys. J.* 93:1895–1905.
3. Yonkunas, M. J., Y. Xu, and P. Tang. 2005. Anesthetic interaction with ketosteroid isomerase: insights from molecular dynamics simulations. *Biophys. J.* 89:2350–2356.
4. Xu, Y., P. Tang, and S. Liachenko. 1998. Unifying characteristics of sites of anesthetic action revealed by combined use of anesthetics and non-anesthetics. *Toxicol. Lett.* 100–101:347–352.
5. Xu, Y., V. E. Yushmanov, and P. Tang. 2002. NMR studies of drug interaction with membranes and membrane-associated proteins. *Biosci. Rep.* 22:175–196.
6. Campagna, J. A., K. W. Miller, and S. A. Forman. 2003. Mechanisms of actions of inhaled anesthetics. *N. Engl. J. Med.* 348:2110–2124.
7. Eckenhoff, R. G., and J. S. Johansson. 1997. Molecular interactions between inhaled anesthetics and proteins. *Pharmacol. Rev.* 49:343–367.
8. Franks, N. P., and W. R. Lieb. 1994. Molecular and cellular mechanisms of general anaesthesia. *Nature.* 367:607–614.
9. Karlin, A. 2002. Emerging structure of the nicotinic acetylcholine receptors. *Nat. Rev. Neurosci.* 3:102–114.
10. Mihic, S. J., Q. Ye, M. J. Wick, V. V. Koltchine, M. D. Krasowski, S. E. Finn, M. P. Mascia, C. F. Valenzuela, K. K. Hanson, E. P. Greenblatt, R. A. Harris, and N. L. Harrison. 1997. Sites of alcohol and volatile anaesthetic action on GABA(A) and glycine receptors. *Nature.* 389:385–389.
11. Unwin, N. 2005. Refined structure of the nicotinic acetylcholine receptor at 4A resolution. *J. Mol. Biol.* 346:967–989.
12. Ma, D., Z. Liu, L. Li, P. Tang, and Y. Xu. 2005. Structure and dynamics of the second and third transmembrane domains of human glycine receptor. *Biochemistry.* 44:8790–8800.
13. Opella, S. J., and F. M. Marassi. 2004. Structure determination of membrane proteins by NMR spectroscopy. *Chem. Rev.* 104:3587–3606.
14. Yushmanov, V. E., Y. Xu, and P. Tang. 2003. NMR structure and dynamics of the second transmembrane domain of the neuronal acetylcholine receptor β 2 subunit. *Biochemistry.* 42:13058–13065.
15. Yushmanov, V. E., P. K. Mandal, Z. Liu, P. Tang, and Y. Xu. 2003. NMR structure and backbone dynamics of the extended second transmembrane domain of the human neuronal glycine receptor α1 subunit. *Biochemistry.* 42:3989–3995.
16. Tang, P., P. K. Mandal, and Y. Xu. 2002. NMR structures of the second transmembrane domain of the human glycine receptor α (1) subunit: model of pore architecture and channel gating. *Biophys. J.* 83:252–262.
17. Szarecka, A., Y. Xu, and P. Tang. 2007. Dynamics of heteropentameric nicotinic acetylcholine receptor: implications of the gating mechanism. *Proteins.* 68:948–960.
18. Johansson, J. S., B. R. Gibney, F. Rabanal, K. S. Reddy, and P. L. Dutton. 1998. A designed cavity in the hydrophobic core of a four-α-helix bundle improves volatile anesthetic binding affinity. *Biochemistry.* 37:1421–1429.
19. Johansson, J. S., D. Scharf, L. A. Davies, K. S. Reddy, and R. G. Eckenhoff. 2000. A designed four-α-helix bundle that binds the volatile general anesthetic halothane with high affinity. *Biophys. J.* 78:982–993.
20. Davies, L. A., Q. Zhong, M. L. Klein, and D. Scharf. 2000. Molecular dynamics simulation of four-α-helix bundles that bind the anesthetic halothane. *FEBS Lett.* 478:61–66.
21. Pidikiti, R., M. Shamim, K. M. Mallela, K. S. Reddy, and J. S. Johansson. 2005. Expression and characterization of a four-α-helix bundle protein that binds the volatile general anesthetic halothane. *Biomacromolecules.* 6:1516–1523.
22. Cui, T., V. Bondarenko, D. Ma, C. Canlas, N. R. Brandon, J. S. Johansson, Y. Xu, and P. Tang. Four-α-helix bundle with designed anesthetic binding pockets. Part II: Halothane effects on structure and dynamics. *Biophys. J.* 94:4464–4472.
23. Farrow, N. A., R. Muhandiram, A. U. Singer, S. M. Pascal, C. M. Kay, G. Gish, S. E. Shoelson, T. Pawson, J. D. Forman-Kay, and L. E. Kay. 1994. Backbone dynamics of a free and phosphopeptide-complexed Src homology 2 domain studied by 15N NMR relaxation. *Biochemistry.* 33:5984–6003.
24. Delaglio, F., S. Grzesiek, G. W. Vuister, G. Zhu, J. Pfeifer, and A. Bax. 1995. NMRPipe: a multidimensional spectral processing system based on UNIX pipes. *J. Biomol. NMR.* 6:277–293.
25. Johnson, B. A. 2004. Using NMRView to visualize and analyze the NMR spectra of macromolecules. *Methods Mol. Biol.* 278:313–352.
26. Goddard, T. D., and D. G. Kneller. SPARKY 3. University of California, San Francisco.
27. Huang, Y. J., G. V. Swapna, P. K. Rajan, H. Ke, B. Xia, K. Shukla, M. Inouye, and G. T. Montelione. 2003. Solution NMR structure of ribosome-binding factor A (RbfA), a cold-shock adaptation protein from *Escherichia coli*. *J. Mol. Biol.* 327:521–536.
28. Hitchens, T. K., J. A. Lukin, Y. Zhan, S. A. McCallum, and G. S. Rule. 2003. MONTE: an automated Monte Carlo based approach to nuclear magnetic resonance assignment of proteins. *J. Biomol. NMR.* 25:1–9.
29. Hitchens, T. K., S. A. McCallum, and G. S. Rule. 2003. Data requirements for reliable chemical shift assignments in deuterated proteins. *J. Biomol. NMR.* 25:11–23.
30. Guntert, P., C. Mumenthaler, and K. Wuthrich. 1997. Torsion angle dynamics for NMR structure calculation with the new program DYANA. *J. Mol. Biol.* 273:283–298.
31. Cornilescu, G., F. Delaglio, and A. Bax. 1999. Protein backbone angle restraints from searching a database for chemical shift and sequence homology. *J. Biomol. NMR.* 13:289–302.
32. Baxter, N. J., and M. P. Williamson. 1997. Temperature dependence of 1H chemical shifts in proteins. *J. Biomol. NMR.* 9:359–369.
33. Humphrey, W., A. Dalke, and K. Schulten. 1996. VMD: visual molecular dynamics. *J. Mol. Graph.* 14:33–38.
34. Koradi, R., M. Billeter, and K. Wuthrich. 1996. MOLMOL: a program for display and analysis of macromolecular structures. *J. Mol. Graph.* 14:51–55.
35. Lefevre, J. F., K. T. Dayie, J. W. Peng, and G. Wagner. 1996. Internal mobility in the partially folded DNA binding and dimerization domains of GAL4: NMR analysis of the N-H spectral density functions. *Biochemistry.* 35:2674–2686.
36. Krizova, H., L. Zidek, M. J. Stone, M. V. Novotny, and V. Sklenar. 2004. Temperature-dependent spectral density analysis applied to monitoring backbone dynamics of major urinary protein-I complexed with the pheromone 2- sec-butyl-4,5-dihydrothiazole. *J. Biomol. NMR.* 28:369–384.
37. Kneller, J. M., M. Lu, and C. Bracken. 2002. An effective method for the discrimination of motional anisotropy and chemical exchange. *J. Am. Chem. Soc.* 124:1852–1853.
38. Fushman, D., S. Cahill, and D. Cowburn. 1997. The main-chain dynamics of the dynamin pleckstrin homology (PH) domain in solution: analysis of 15N relaxation with monomer/dimer equilibration. *J. Mol. Biol.* 266:173–194.
39. Lipari, G., and A. Szabo. 1982. Model-free approach to the interpretation of nuclear magnetic resonance relaxation in macromolecules. 1. Theory and range of validity. *J. Am. Chem. Soc.* 104:4546–4559.
40. Lipari, G., and A. Szabo. 1982. Model-free approach to the interpretation of nuclear magnetic resonance relaxation in macromolecules. 2. Analysis of experimental results. *J. Am. Chem. Soc.* 104:4559–4570.
41. Mandel, A. M., M. Akke, and A. G. Palmer III. 1995. Backbone dynamics of *Escherichia coli* ribonuclease HI: correlations with structure and function in an active enzyme. *J. Mol. Biol.* 246:144–163.

42. Loria, J. P., M. Rance, and A. G. Palmer. 1999. A relaxation-compensated Carr-Purcell-Meiboom-Gill sequence for characterizing chemical exchange by NMR spectroscopy. *J. Am. Chem. Soc.* 121:2331–2332.

43. Tollinger, M., N. R. Skrynnikov, F. A. Mulder, J. D. Forman-Kay, and L. E. Kay. 2001. Slow dynamics in folded and unfolded states of an SH3 domain. *J. Am. Chem. Soc.* 123:11341–11352.

44. Tang, P., J. Hu, S. Liachenko, and Y. Xu. 1999. Distinctly different interactions of anesthetic and nonimmobilizer with transmembrane channel peptides. *Biophys. J.* 77:739–746.

45. Xu, Y., and P. Tang. 1997. Amphiphilic sites for general anesthetic action? Evidence from ^{129}Xe-{^{1}H} intermolecular nuclear Overhauser effects. *Biochim. Biophys. Acta.* 1323:154–162.

46. Suhre, K., J. Navaza, and Y. H. Sanejouand. 2006. NORMA: a tool for flexible fitting of high-resolution protein structures into low-resolution electron-microscopy-derived density maps. *Acta Crystallogr.* 62:1098–1100.

47. Suhre, K., and Y. H. Sanejouand. 2004. ElNemo: a normal mode web server for protein movement analysis and the generation of templates for molecular replacement. *Nucleic Acids Res.* 32:W610–W614.